



Quality characteristics and analysis of input parameters on laser beam welding of hairpin windings in electric drives

Markus Omlor¹ · Niklas Seitz¹ · Tom Butzmann¹ · Tobias Petrich¹ · Rolf Gräf¹ · Ann-Christin Hesse² · Klaus Dilger²

Received: 24 October 2022 / Accepted: 11 February 2023 / Published online: 10 March 2023
© The Author(s) 2023, corrected publication 2023

Abstract

The relevance of electric drives in individual mobility is continuously increasing. This requires the use of new manufacturing processes in automotive production. In modern stators, the so-called hairpin winding is used. The production process entails rectangular copper conductors (hairpin) to be contacted by laser beam welding. To avoid temperature peaks due to resistance heating in the current-carrying wire, a high cross-sectional area in the welding seam is required. Therefore, the pore volume must be considered. This is proven by thermographic investigations of electrically stressed hairpin connections. To optimize the welding process, effects of the previous manufacturing steps and the welding parameters themselves must be taken into account. This paper analyses systematically the impact of all translational and rotational deviations on the corresponding welding quality. The tests are performed by using a disk laser. A laser spot with a focus diameter of 170 μm is compared to a statically shaped beam, capable of distributing power in core and ring beam. As an additional parameter, the influence of oxygen content in the copper wire is investigated by using electrolytic tough pitch copper (Cu-ETP) and oxygen-free copper (Cu-OF). Furthermore, the interaction between an additional cutting step before contacting and the welding path is considered. X-ray computed tomography (CT) is used to analyse the welding quality. The main finding of the studies is the significant influence of the gap and height offset between the wire ends on the resulting cross-sectional area. In addition, a low oxygen content of the copper and the use of static beam shaping reduce weld spatters, porosity and increase process stability. Three geometries in the welding path perform better in gap bridging and cause less spatters.

Keywords Electric drives · Hairpin winding · Laser beam welding · Copper · Automotive

Recommended for publication by Commission IV - Power Beam Processes

✉ Markus Omlor
markus.omlor@porsche.de

Niklas Seitz
niklas.seitz1@porsche.de

Tom Butzmann
tom.butzmann1@porsche.de

Tobias Petrich
tobias.petrich@porsche.de

Rolf Gräf
rolf.graef@porsche.de

Ann-Christin Hesse
a.hesse@tu-braunschweig.de

Klaus Dilger
k.dilger@tu-braunschweig.de

¹ Dr. Ing. h.c. F. Porsche AG, Stuttgart, Germany

² Technische Universität Braunschweig, Brunswick, Germany

Nomenclature

| | |
|------------------------|---|
| $A_{\varphi=90^\circ}$ | Cross-sectional area $\varphi = 90^\circ$ |
| $A_{\varphi=90^\circ}$ | Average cross-sectional area $\varphi = 90^\circ$ |
| ANOVA | Analysis of variance |
| BLW | BrightLine Weld (static beam shaping by Trumpf) |
| CT | X-ray computed tomography |
| Cu-ETP | Electrolytic tough pitch copper |
| Cu-OF | Oxygen free copper |
| CW | Clockwise |
| CCW | Counter-clockwise |
| d_f, d_{f-out} | Focal diameters |
| GEO 1 | Welding parameter with 1 geometry |
| GEO 3 | Welding parameter with 3 geometries (level 1) |
| I_p | Test current |
| k | Coefficient for regression model $A_{\varphi=90^\circ}$ |
| j | Coefficient for regression model N_{Sp} |
| $N_{1,2,3}$ | Number of welding path |
| N_{Sp} | Number of spatters |
| R | Resistance of conductor |

| | |
|----------------|--|
| R_D^2 | Coefficient of determination |
| RoI | Region of interest in CT-analysis |
| SS | Sum of squares |
| SSP | Single spot welding |
| t_p | Process time of welding |
| T | Temperature of conductor |
| T_{max} | Maximum temperature of conductor |
| V_{Cu} | Melting volume |
| V_p | Pore volume |
| V_{Pmax} | Volume largest pore |
| Δx | Welding gap |
| Δy | Lateral offset |
| Δz | Height offset |
| α | Rotation around x |
| α_{1-4} | Significance level |
| β | Rotation around y |
| γ | Rotation around z |
| σ | Standard deviation |
| φ | Rotation angle of cross-sectional area |

1 Introduction

1.1 Hairpin technology

Stricter climate protection targets and the associated specifications for pollutant emission values and fleet consumption targets are encouraging car manufacturers to further develop alternative drive concepts and make them marketable. Forecasts show a 33% sales share of electric vehicles in a medium scenario in 2030 [1, 2]. This is accompanied by the development of new production environments and processes. A hairpin winding, which differs from conventional round wire windings by the rectangular cross-section of the copper conductor, has become the standard in stator production (Fig. 1). Thereby, a higher copper fill factor is

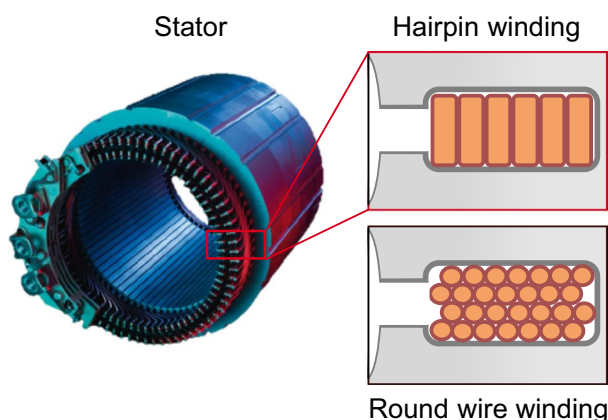


Fig. 1 Hairpin winding and round wire winding in a stator slot (stator: [5])

achieved in the stator slots, resulting in higher performance and efficiency while maintaining the same volume [3, 4].

The manufacturing process of hairpin stators can be fully automated and requires several production steps before the hairpin ends can be contacted together. Laser beam welding has become the established method for the contacting process [6–10]. It is particularly important that the conductor ends are sufficiently bonded so that the requirements for electrical conductivity and mechanical strength are fulfilled. Furthermore, spatters must be avoided to prevent damage to other components.

The copper wire is wound on coils and insulated with a high-temperature-resistant thermoplastic, e.g. polyetheretherketone (PEEK). After the copper wire is unwound and straightened in vertical and horizontal direction, the insulation is removed from the wire ends in a stripping process to provide a blank copper surface in the welding area. To achieve a low cycle time and high process stability, this is usually realised by mechanical milling of the insulation or stripping with the use of a laser beam. In a punching process, the copper flat wire is cut to the required length within the stripped area. The cutting tool creates a chamfer on all four sides. This contour is needed for the assembly process of the hairpins into the laminated core and prevents damage to the slot insulation and stator slot. To form a hairpin shape from the straightened wire rods, the wire is bent by die bending, swivel bending or free-form bending. A combination of several bending processes is also possible. Before the hairpins are inserted into the laminated core, a special slot liner made of plastic films and aramid paper layers is placed inside the stator slots. In the next production step, the hairpins, which differ in length and bending geometry depending on their position in the stator, are pre-assembled and inserted into the laminated core. To create a hairpin winding, the conductor ends must be bent in the right welding position, which is done by two further bending processes. The ends are first radially expanded and then tangentially twisted into their final position. An S-shaped geometry is created [8, 11].

Before laser beam welding, the pins are clamped in a defined position. However, due to the tolerances in the bending processes and tools, deviations occur in the positioning. This can influence the welding process. In some cases, the height offset is compensated by an additional process step, in which the conductor ends are cut again, while the welding tool is in the clamped state [11, 12]. The cutting can be realized by a shear cut or milling. This leads to the question, which positional deviations can be tolerated by a suitable welding parameter and whether an additional cutting process is required in the hairpin production.

1.2 Electrical contacting

Due to its high electrical conductivity, copper is used in hairpin stators to create a winding. The property of electrical conductivity is directly coupled to the thermal conductivity

of a material by Wiedemann–Franz’s law (constant ratio of electrical and thermal conductivity). The high thermal conductivity and low absorption coefficient in the infrared wavelength range of copper require high energy density during welding and thus high laser power with high beam quality. Untreated copper surfaces reflect about 95% of radiation with infrared wavelengths, while only 5% is absorbed by the copper. A threshold value of about $10 \text{ kW} \cdot \text{mm}^{-1}$ must be achieved to get a deep penetration welding process [13]. As a result, the absorption in the keyhole increases due to multiple reflections and is about 70% [14]. Deep penetration welding with different scanning strategies is used to ensure low welding times and thus minimal heat input in the components [6–10].

During deep penetration welding, metal vapor escapes via the keyhole, which, due to the welding speed and the resulting transverse momentum, can cause the escaping metal vapor to eject parts of the melt volume as spatter. To prevent this, static beam shaping, which allows flexible distribution of laser power in ring beam and core beam, shows potentials. The additional energy input in the ring enlarges the keyhole opening, allowing the metal vapor to escape more easily and less melt to accumulate behind the keyhole. This enables low-spatter welding even at high feed rates. If the deep welding process cannot be maintained or if the keyhole is too small for the amount of escaping gases, process-related pores can form in the solidification zone of the melt [15, 16].

To build a hairpin stator, more than 100 welds must be performed on the conductor ends. Any form of contamination on the copper surfaces, such as insulation residues, results in spatter formation and an unstable welding process. Due to the high energy input during the welding process, residues burn in a very short time, causing evaporation. The resulting gases can eject parts of the molten volume or remain as pores in the weld [17].

Gläsel [10, 18] investigates the quality of laser-contacted hairpins using four-wire measurement to determine electrical resistance. The conductor resistance can thus be directly related to the efficiency of the stator. A disadvantage of this method is that a high number of repetitions is required for sufficient accuracy. Especially in the case of positional deviations, the shape of the welds can vary considerably, causing the distance of the voltage measurement to differ. This leads to inaccuracies that may not be detected. In addition, the test method cannot be used with welded hairpins in the stator.

Gläsel [10] also takes positional deviations into account. In particular, the X- and Y-translations are identified as influencing variables in the resistivity measurement. For a gap up to $\Delta x = 0,5 \text{ mm}$, the resistance increases linearly, which is justified by the smaller cross-sectional area of the joint. With Y-offset and Y-rotation, a lower melt volume is resulting, which also increases the

resistance of the welded joint. For height offset, Gläsel sets the focus of the laser beam on the lower pin and cannot detect any change in resistance up to $\Delta z = 6 \text{ mm}$ for the welding parameter used.

So far, the advantages of static beam shaping have not been investigated for hairpin welds with positional deviations, showing potentials in high welding speeds, low spatter formation [15, 16] and good gap bridging [19]. In association with the porosity, the influence of the oxygen content of the copper used will also be considered in subsequent examinations. Toth [20] has already demonstrated a significant influence of oxygen content in electron beam welding (vacuum) of hairpins. As different welding paths interact differently with the positional deviations, this is also examined coherently.

To achieve holistic conclusions about the welding process, X-ray computed tomography (CT) is utilised to analyse the welded samples. This method is also feasible for the entire stator assembly. The quality characteristics of molten copper volume, cross-sectional area and porosity can be evaluated. Porosity is particularly important for the investigation of beam shaping and oxygen content of the copper. Through the complementary use of high-speed imaging during welding, spatters can also be detected.

2 Methods and materials

2.1 Materials

The oxygen content of the copper material used has an influence on the weldability of copper. Impurities in the copper reduce the conductivity, that is why oxygen is added to many types of copper during refinement. It oxidises impurities but leads to the formation of copper oxide in the microstructure. If hydrogen is contained in the welding environment, this can cause brittleness and cracking due to hydrogen disease [21].

The solubility of oxygen in copper is a relevant factor, too. Horrigan [22] reveals that with higher temperatures the solubility of oxygen increases and thus the formation of copper oxide is enhanced. Due to the high temperature input during the welding process, a high amount of oxygen is dissolved in the melt, which can lead to metallurgic pores during the cooling process. Table 1 compares the material properties of low-oxygen CU-ETP with oxygen-free CU-OF. As both copper materials have a high electrical conductivity of $> 58 \text{ m} \cdot \Omega^{-1} \cdot \text{mm}^{-2}$ and a low oxygen content, they are used in the production of hairpin stators [21]. In these investigations the oxygen content of Cu-ETP was measured with 0,021%.

Table 1 Mass fractions of copper (Cu) and oxygen according to DIN EN 1977 [23]; Comparison of Cu-ETP and Cu-OF (* Defined by requirements for resistance to hydrogen)

| Mass fraction (%) | Cu-ETP | | Cu-OF | |
|-------------------|--------|-------|--------|-----|
| | CW004A | | CW008A | |
| | min | max | min | max |
| Cu | 99,90 | - | 99,95 | - |
| O | - | 0,040 | - | * |

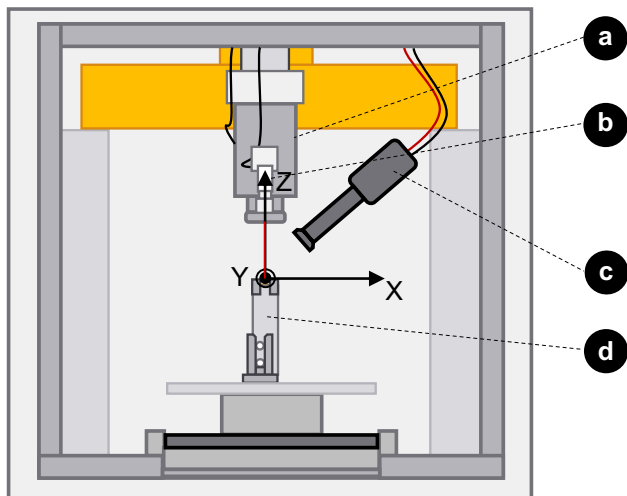


Fig. 2 Schematic layout of the laser beam welding system (based on [26]); **a** Optics; **b** Photodiode for recording of discrete beamspectrum; **c** High-speed camera; **d** Welding fixture

2.2 Laser beam welding

Laser beam welding is realised by a disk laser with maximum power of 6000 W (TruDisk6001 by Trumpf, Ditzingen, Germany). BrightLine Weld BLW is used for static beam shaping (Trumpf, Ditzingen, Germany). The laser optics (PFO 33–2 f255 by Trumpf, Ditzingen, Germany) is mounted on a movable portal axis in the upper part of the system Fig. 2a. Attached to the optics are a high-speed camera (FASTCAM Nova S9 by Photron, San Diego, USA) Fig. 2c for recording the welding process, a camera in the beam path for positioning and a photodiode for quantifying the laser reflection (LWM 4.0 by Precitec GmbH & Co. KG, Gaggenau, Germany) Fig. 2b. A computer unit analyses the images from the high-speed camera for automated spatter count evaluation by using difference images. A spatter is counted if 30 or more contiguous pixels exceed a grey value difference. For this reason, even spatters with diameters $> 10 \mu\text{m}$ are counted, which can result in a high detected number of spatters per process [24, 25]. Also, the computer controls the photodiode for process monitoring and stores all measurement data. A workpiece carrier provides the fixation

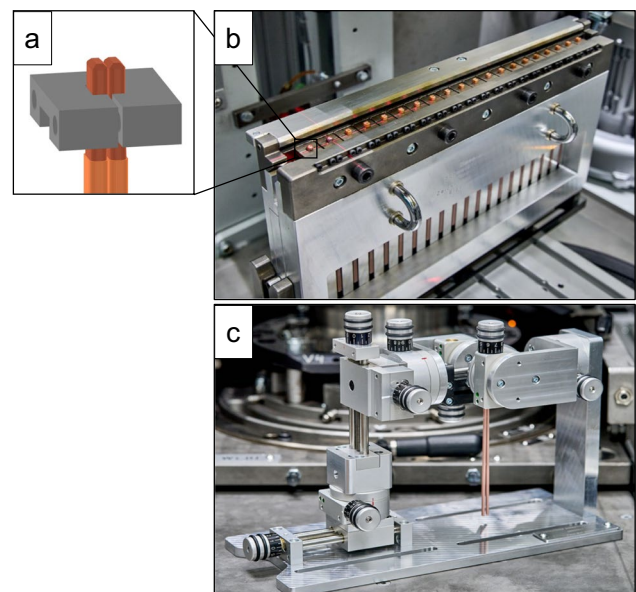


Fig. 3 Welding fixtures; **a** Hairpin pair in one clamping tool [26]; **b** fixture with no degrees of freedom, 20 pairs of hairpins [26]; **c** fixture with 3 translational and 3 rotational degrees of freedom, 1 pair of hairpins

and positioning of the stators. To allow easier examination of the welding process, the stator is replaced by a fixture Fig. 2d for clamping individual pins.

For the following investigations, two welding fixtures for single pin pairs are utilised, which are shown in Fig. 3. To perform welding tests with multiple pins, the fixture without degrees of freedom for the pin position is used. The fixture (b) allows 20 pin pairs to be clamped. Each pin pair is clamped in the fixture by two clamping jaws (a) made of tungsten-copper Class E 80/20 with a thermal conductivity of $\kappa = 170 \text{ W} \cdot \text{m}^{-1} \cdot \text{K}^{-1}$. A zero gap is achieved by a constant clamping force so that the two copper conductors have no translations or rotations relative to each other. For welds with positional deviations of the two pins, the fixture (c) is used. This fixture provides the ability to clamp a pair of pins and adjust the position of the two copper conductors relative to each other in six degrees of freedom. Welding tests with positional deviations can be performed through adjustment screws with fine thread and a resolution of 0,05 mm. Rotational adjustment has a resolution of $0,75^\circ$. The jaws of both fixtures have the same contact area with the conductor end, as well as the same material, volume and heat capacity.

To investigate the influence of an additional cutting process of the hairpins on the welding process, welds with cut and uncut hairpins are performed. Figure 4 pictures the surface of cut and uncut hairpin ends. “Cut pins” are cut to an identical height just before welding and show a flat surface over the entire conductor cross-section. “Not-cut hairpins” in contrast have a circumferential chamfer, which is produced

by the punching tool, and is used for joining in the laminated core.

Two different welding paths are utilised for the following investigations (Fig. 5). The parameter GEO 3 is used as an initial parameter: Three welding geometries are programmed for GEO 3, which are dimensioned according to the chamfer of uncut hairpins. First, in N_1 (Dimensions: 2,4 mm • 1,2 mm), the left hairpin is melted in an elliptical weld geometry, while the right hairpin is passively heated by heat conduction. Then, the right hairpin is melted with the same geometry and — due to the already high temperature of the copper — fewer repetitions in N_2 . During N_2 , the two liquid melts already combine with each other and create a common melt pool, forming a bridge between the hairpins. N_1 and N_2 are processed in opposite directions. Geometry N_3 (Diameter: 1,6 mm) increases the melt volume to obtain a sufficient connection area. An ellipse can lead to energy hotspots in the reversal points at high velocities. To prevent this energy input maxima in the gap, a circular geometry is chosen for N_3 [26]. Due to the higher absorption of liquid copper, less laser power is used for N_3 . Table 2 lists the welding parameters. In addition to the initial parameter (GEO 3), another welding parameter (GEO 1) is developed for comparison, using only one welding geometry N_1 . The number of geometry repetitions is chosen so that the melt volume of GEO 1 is in the same range as the melt volume of GEO 3 under the same input conditions (without positioning deviations). Although the energy input is thus not identical, the

effect of the different welding paths can be better compared due to the same melting volume. The parameters in Table 2 are listed for a single spot welding (SSP) process with a laser focus diameter of $d_f=0,17mm$.

With the use of static beam shaping (BLW) an outer ring with the focus diameter $d_{f.out}=0,68mm$ is added to the inner spot ($d_f=0,17mm$). Therefore, one specific intensity distribution with 60% of the laser power in the outer ring and 40% in the inner ring is compared to the SSP parameter. This is implemented only for the welding path GEO 3. To reach the similar melting volume despite the higher spot size comparing to SSP, the maximum laser power and the geometry repetitions must be increased. The parameters that change from SSP to BLW are listed in Table 3.

2.3 X-ray CT

The analysis of the welding results is performed by X-ray computed tomography (CT) (HMX ST 225 by Nikon Metrology, Tring, UK). Figure 6 illustrates the evaluation method used [27]. The hairpin pairs are fixed individually on a rotatable fixture and X-rayed. By capturing many individual images of the rotating welded joints, a three-dimensional image of each welded joint can be generated using image transformation. For this purpose, the pixels are assembled into cube-shaped voxels with an edge length of 28 μm . Pores are detected from a volume of $3 \cdot 3 \cdot 3$ voxels ($> 590 \cdot 10^{-6} mm^3$), that fall below a specific gray value.

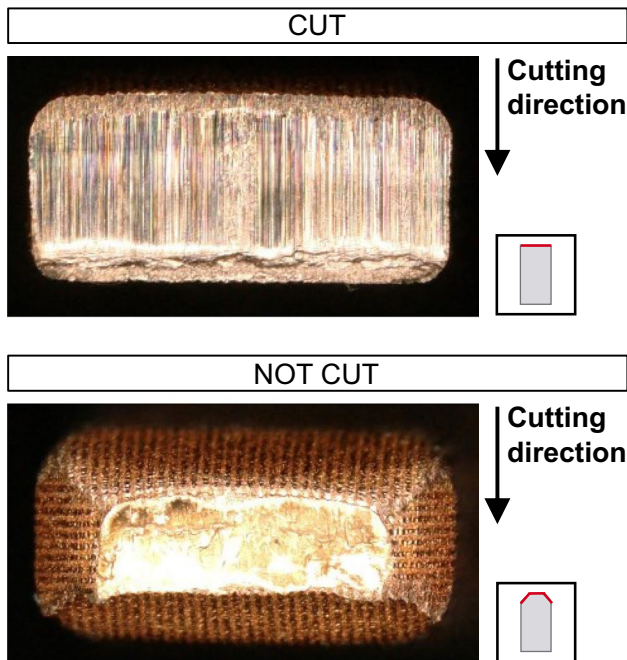


Fig. 4 Surface of cut and not cut conductor ends

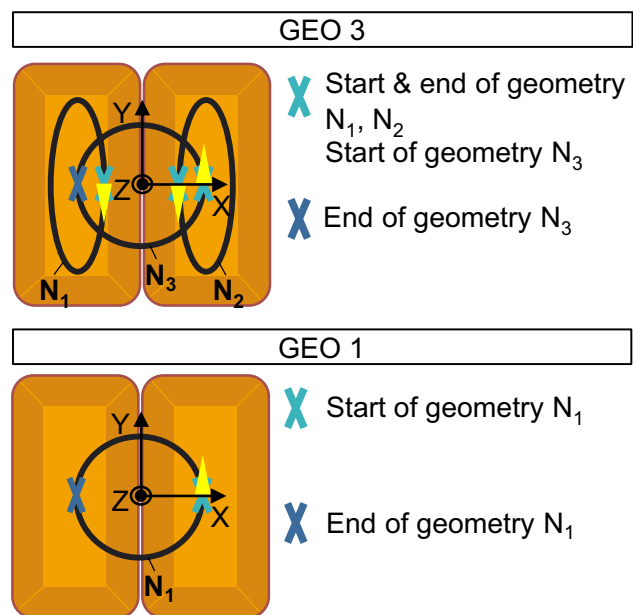


Fig. 5 Welding path of GEO 3 and GEO 1

Table 2 Welding parameters of welding path GEO 3 and GEO 1 for single spot welding (SSP)

| Welding parameters | GEO 3 | | | GEO 1 |
|---|-------|-------|-------|-------|
| | N_1 | N_2 | N_3 | N_1 |
| Designation of geometry | N_1 | N_2 | N_3 | N_1 |
| Maximum laser power [W] | 4500 | 4500 | 4000 | 4000 |
| Welding speed [$\text{mm} \cdot \text{s}^{-1}$] | 750 | 750 | 500 | 750 |
| Direction | CW | CCW | CCW | CCW |
| Laser power at start [W] | 900 | 900 | 1800 | 900 |
| Laser power ramp length [ms] | 6,9 | 6,9 | 4,5 | 8,4 |
| Number of geometry repetitions | 5 | 4 | 4,5 | 14 |

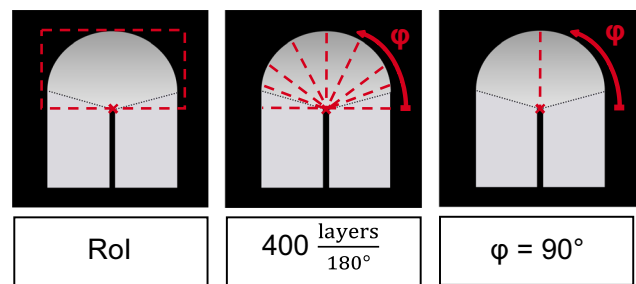
To investigate the quality characteristics, a rectangular region-of-interest (RoI) is placed over the entire welding seam starting from the weld root of each joint. Within the RoI, the cross-sectional areas of the welded joint are calculated on 400 levels at the rotation angle $\varphi = 0 \dots 180^\circ$, which allows the minimum connection area to be output. For better comparability of the welding parameters, the 90° cross-sectional area $A_{\varphi=90^\circ}$ is evaluated in the following. The determined cross-sectional areas only represent the copper surface. Pores contained in the microstructure are already subtracted. In addition, the evaluation methodology calculates the melt volume V_{Cu} , total pore volume V_p and volume of the largest pore V_{Pmax} . Because the melt line does not run in a straight line, a deviation occurs in the quantification of the melt volume. This is negligible for the comparability of the melt volume.

2.4 Thermography of electrically stressed contacts

The contact point of welded hairpins is exposed to high electrical loads during operation. An insufficient contact area leads to a heat hotspot. This can result in overheating and thus in lower retrievable power. In order to investigate the influence of the welding quality on the temperature load, individual contact points of different quality levels will be electrically stressed. During this process, the temperature is measured by a thermographic camera, which records the distribution of local spectral radiation, as well as its change over time in an image field. The underlying principle is the thermal self-radiation of the measured objects, as each body above absolute zero emits thermally excited electromagnetic radiation [28].

Table 3 Modified welding parameters of welding path GEO 3 with static beam shaping (BLW) in comparison to GEO 3 single spot welding (SSP)

| Welding parameters GEO 3 | Single spot welding (SSP) | | | Static beam shaping (BLW) | | |
|--------------------------------|---------------------------|-------|-------|---------------------------|-------|-------|
| | N_1 | N_2 | N_3 | N_1 | N_2 | N_3 |
| Designation of geometry | N_1 | N_2 | N_3 | N_1 | N_2 | N_3 |
| Maximum laser power [W] | 4500 | 4500 | 4000 | 6000 | 6000 | 5500 |
| Laser power at start [W] | 900 | 900 | 1800 | 1200 | 1200 | 2400 |
| Number of geometry repetitions | 5 | 4 | 4,5 | 8 | 6,5 | 4,5 |

**Fig. 6** Method of CT analysis; **a** Region of interest; **b** 400 layers by rotation angle $\varphi = 180^\circ$; **c** cross section at rotation angle $\varphi = 90^\circ$ [27]

In addition to the parameter set of level 1 (GEO 3 SSP), three further quality levels (levels 2 to 4) are manufactured, which have a reduced connection area. These are produced by gradually reducing the laser power. Furthermore, a quality level (level 5) with increased pore volume in the weld seam is used. Pores can especially be caused by insulation residue after an incorrect stripping process [17]. The cross-sectional area at $\varphi = 90^\circ$ of quality level 5 has an average value between quality levels 1 and 2. Table 4 shows the laser power used and the average cross-sectional area of six welded hairpins of each quality level.

Figure 7a shows the circuit diagram of the test setup. A defined test current ($I_p = 150,8 \text{ A}$) is passed through the welded hairpins, represented as resistor R , for a measurement time of 120 s. The parameters are selected so that level 1 reaches a maximum temperature T_{max} of 180°C . To achieve the required test current, nine current sources are connected in parallel. All current sources are connected to a control signal, and each emits the same amount of current. Figure 7b pictures the test setup with the thermographic camera (A400 by FLIR, Wilsonville, USA). The welded hairpins (02) are placed in a free-standing holder perpendicular to the thermographic camera (01) and connected to the current sources via a clamp connection (03). During the experiment, the current sources and the camera are started simultaneously. The welded conductor ends are at room temperature at the beginning of the measurement. Figure 7c shows the image output by the camera. The temperature maximum is marked.

For a temperature measurement by the thermographic camera, a determination of the surface-emissivity is necessary. As metallic surfaces (especially copper) have a very

Table 4 Quality levels used in test series A (Welding parameters: GEO 3, SSP) (Hairpins: Not cut, Cu-OF) (The listed laser power is the max laser power for N_1 and N_2 . The laser power of N_3 for levels 2 to 4 is reduced with the same factor as N_1 and N_2 .)

| Quality Level | 1 | 2 | 3 | 4 | 5 |
|---|------|------|------|------|------|
| Laser Power [W] | 4500 | 3500 | 3400 | 3150 | 4500 |
| $\bar{A}_{\varphi=90^\circ}$ [mm ²] | 9,30 | 4,19 | 4,01 | 1,11 | 7,38 |
| CT-Scan | | | | | |

poor emissivity, which varies depending on the surface condition [29], the welds are painted with a matte black colour. The emissivity is determined in a reference measurement with a sample of known emissivity (reference sample). For this purpose, both samples (reference sample and hairpin sample) are heated to a known temperature. After that, the temperature is measured on the reference sample. Next, the same measurement area of the thermographic camera is positioned on the painted surface of the hairpin. The emissivity is then adjusted in software so that the temperature of the hairpin sample corresponds to the temperature of the reference sample. The determined emissivity for coated hairpins is 0,93.

2.5 Methodical approach

The connection area of the hairpin created by laser beam welding (Section 2.2) is exposed to continuous vibrations in the

vehicle and electromechanical stress, as well as thermal stress due to the current flow. The temperature measurement of electrically stressed hairpins by the presented method (Section 2.4) is supposed to show the importance of the quality characteristic “cross-sectional area $A_{\varphi=90^\circ}$ ” (test series A). Therefore, the X-ray CT is used as a measurement method (Section 2.3).

In test series B1, the influence of using static beam shaping (BLW) compared to single spot welding (SSP) and oxygen content of the copper material is examined. Both factors particularly influence the pore formation during the welding process (Section 2.1). A full factorial trial design is applied in Table 5. Each combination is repeated ten times without positional deviations (ideal position). Furthermore, in a second trial section B2, the tolerance of the process parameters is shown for each translational and rotational degree of freedom in a Cartesian coordinate system for both variants of the beam shape. Only Cu-OF is used here. This enables the identification of the significant positional deviations for the welding process.



Fig. 7 Thermography of electrically stressed hairpin contacts; **a** circuit diagram; **b** experimental setup; **c** output image of the camera

The relevant positional deviations (gap, height offset) from test series B2 are transferred into test series C. The structure of the trial design is shown in Table 6. The factors of the conductor end geometry as well as the welding path of the parameters GEO 1 and GEO 3 are investigated in a full factorial design of experiments. For each factor combination, the gap and height offset are added as a centrally composed design (Fig. 8). Since height offset cannot occur with cut pins, these experiments are performed by varying the gap only. To minimize the influence of other factors, the experiment is conducted using single spot welding and Cu-OF. Each factor combination is repeated three times.

3 Results

3.1 Derived quality characteristics of thermal imaged hairpin welds (Test series A)

The diagrams in Fig. 9 show the results of the thermographed, electrically stressed hairpins. For the evaluation, the temperature of the welded joints after 120 s is analysed. The diagram in Fig. 9a displays the mean values as well as the minimum and maximum temperature values of the individual quality levels. The mean value of the temperature increases significantly ($\alpha_j = 0,05$; ANOVA: Appendix 1) with increasing quality level (levels 1 to 4). The value is 10% higher at level 4 compared to level 1. It is noted that the scattering of the levels decreases with increasing temperature. Temperature values achieved by quality level 5 are within a range between quality levels 1 and 2. These results can be explained by the measured cross-sectional areas. The diagram in Fig. 9b shows the temperatures reached, as a function of the cross-sectional area at $\varphi = 90^\circ$ of the individual hairpins. It is proven that the temperature of the welded joint increases with decreasing connection area.

This correlation can be explained by Joule heating (Joule’s first law). The electrical power P_{el} is calculated from the product of the voltage and the current I . Adding the Ohm’s law and the resistance of a conductor R to the

Table 6 Trial design of test series C

| Test series C | | | |
|------------------------------------|-----------------------|---|--------------------|
| Geometry of conductor end (Fig. 4) | Welding path (Fig. 5) | Gap [mm] | Height offset [mm] |
| Cut | GEO 3 | Only gap variation in intervals of Fig. 8 | |
| | GEO 1 | | |
| Not cut | GEO 3 | Central composite design (Fig. 8) | |
| | GEO 1 | | |

equation with the length l , cross-section A and specific electrical resistance ρ , it results in the following:

$$P_{el} = R \cdot I^2 = \frac{\rho \cdot l}{A} \cdot I^2 \tag{1}$$

In combination with Joule’s first law (time t , electric potential energy E_{el} , heat Q):

$$Q = E_{el} = \frac{\rho \cdot l}{A} \cdot I^2 \cdot t \tag{2}$$

If Eq. (2) is joined with the basic equation of thermodynamics (specific heat capacity c , mass m)

$$Q = c \cdot m \cdot \Delta T \tag{3}$$

it becomes clear that the temperature change ΔT of a conductor due to electric current increases indirectly proportional with the decrease of the cross-sectional area A :

$$\Delta T \sim \frac{1}{A} \tag{4}$$

Table 5 Trial design of test series B1

| Test series B1 | | |
|------------------------------------|-----|--------------------------|
| Beam shape | | Type of copper (Table 1) |
| Power ring: 60% Power core: 40% | BLW | Cu-ETP Cu-OF |
| Power ring: 0% Power core: 100% | SSP | Cu-ETP Cu-OF |

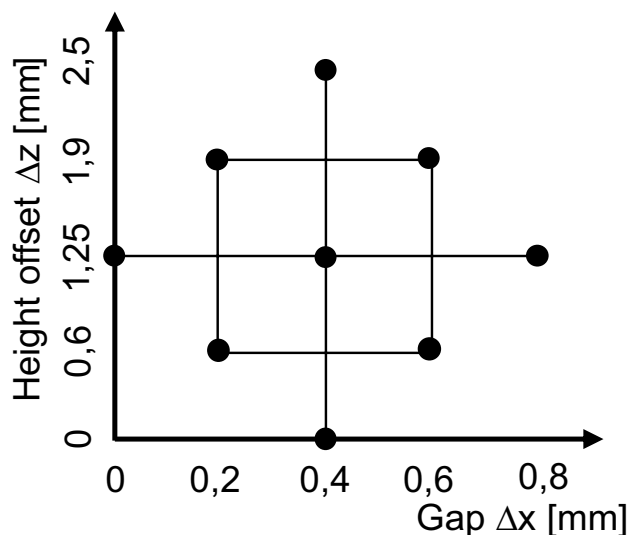
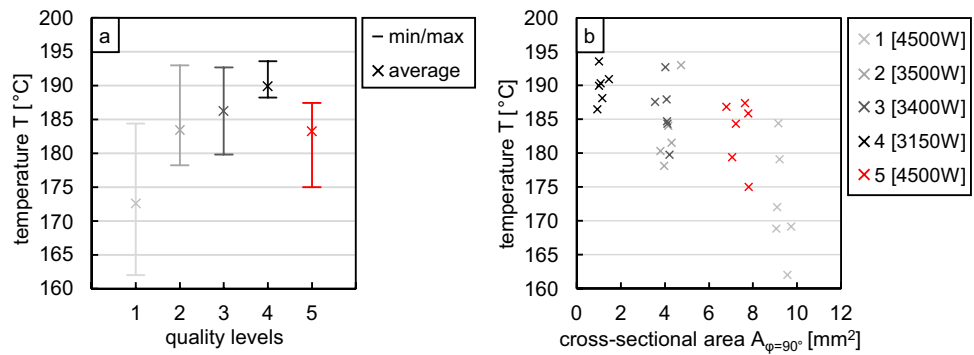


Fig. 8 Central composite design in trial design of test series C

Fig. 9 Temperature in the welding seam after 120 s as a function of **a** the quality level and **b** the cross-sectional area at $\varphi = 90^\circ$



These results underline the relevance of the cross-sectional area as a quality characteristic. A connection area larger than the cross-sectional area of the copper conductors should always be targeted in order to avoid thermal losses in the electric machine. Furthermore, it should be considered that pores reduce the connection surface.

3.2 Impact of oxygen content, static beam shaping and all positional deviations (Test series B1 and B2)

Test series B1 investigates the influence of beam shaping and oxygen content on the welding process. Both factors show a significant influence on the total pore volume, volume of the largest pore and the number of spatters — the interaction is not significant ($\alpha_2 = 0,05$; ANOVA: Appendix 2). Figure 10 presents the results in form of boxplot diagrams. Diagram (a) points out that the use of Cu-OF reduces the total pore volume V_p in SSP by 40,4% on average compared to Cu-ETP. By using BLW, the total pore volume is further reduced to an average value of 0,055 mm^3 for Cu-OF. This equates to a 67,7% reduction compared to SSP.

Diagram (b) reflects similar results. It can also be seen from the volume of the largest pore V_{Pmax} that with BLW and the use of Cu-OF the lowest pore formation occurs

($V_{Pmax} < 0,05 \text{ mm}^3$). In contrast, the volume of the largest pore V_{Pmax} with SSP and Cu-OF amounts to 0,124 mm^3 on average. The scattering width increases substantially with the use of SSP indicating a less stable process.

The number of weld spatters N_{sp} in diagram (c) illustrates that the lowest number of spatters occurs with BLW and Cu-OF. For SSP and Cu-OF, the number of spatters is 71,4% higher.

The increased oxygen content in Cu-ETP leads to metallurgical pores, which are exemplified in a CT image of a Cu-ETP hairpin in Fig. 11. Metallurgical pores are characterized by their smaller volume and high number in the entire welding area [30, 31]. The escaping gases at the keyhole create undesirable weld spatters during the welding process, as the gas can only escape with difficulty from the keyhole. This instability in the keyhole results in large process pores remaining in the weld seam. The formation of process pores in line welds is mostly described by a detachment from the keyhole [30, 31].

By using Cu-OF, fewer metallurgical pores are formed. If the keyhole is enlarged at the surface by the additional energy input in ring form (BLW), less weld spatters are produced and less pores remain in the microstructure. The escape of gases in the welding process is improved. Figure 12a explains the function of BLW compared to SSP in

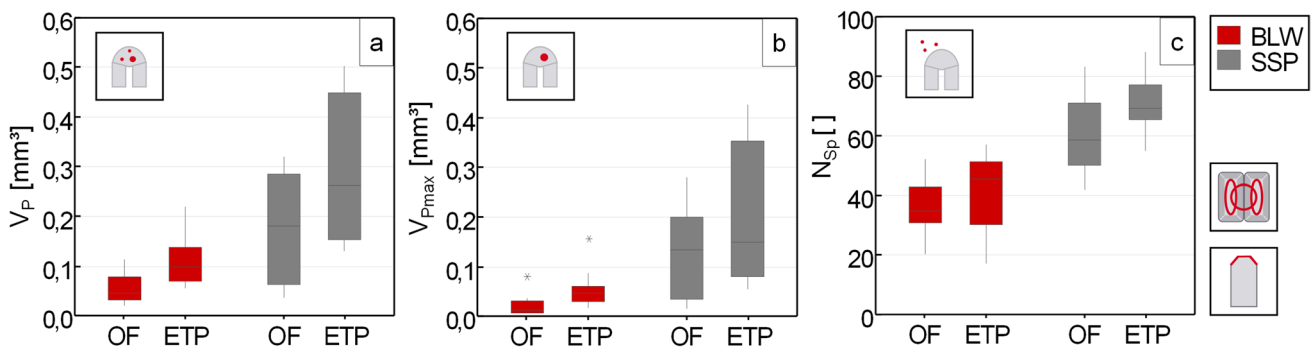


Fig. 10 Variation of oxygen content and beam shape; **a** pore volumes V_p ; **b** volume of the largest pore V_{Pmax} ; **c** number of spatters N_{sp} (Welding parameters: GEO 3—SSP und GEO 3—BLW) (Hairpins: Not cut, Cu-ETP and CU-OF)

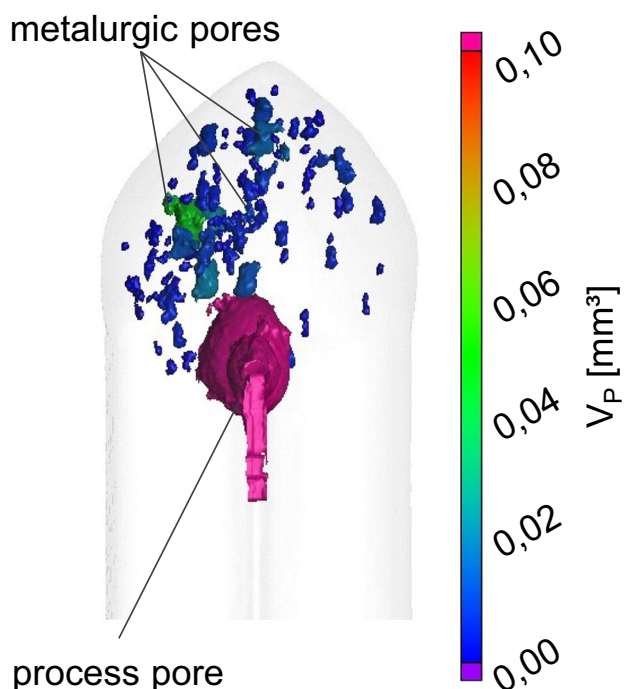


Fig. 11 CT-visualisation of porosity in a welded hairpin joint (Cu-ETP)

a schematic diagram. Figure 12c images the spot size. The high-speed image in Figure 12b shows the widened keyhole

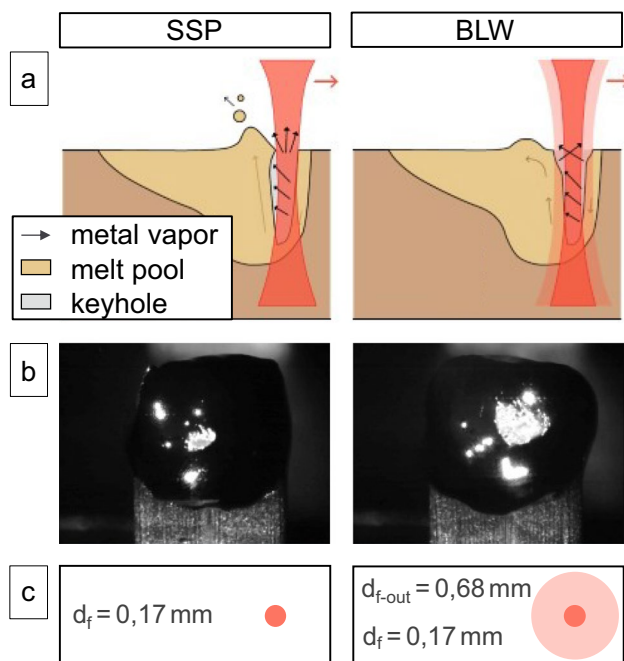


Fig. 12 a Schematic illustration of SSP and BLW (based on [32]); b High-Speed image of SSP and BLW; c Spot sizes of SSP and BLW.

(right) in a real image compared to the smaller keyhole opening (left).

Test series B2 is designed to identify relevant positional deviations on the welding process with process parameter GEO 3 for SSP and BLW. Based on test series B1, only uncut Cu-OF hairpin pairs are used. For this purpose, the welding fixture with six degrees of freedom is utilised to investigate all rotational and translational degrees of freedom independently. The welding paths are changed for each positional deviation so that N_1 and N_2 are shifted with the hairpins and are thus always centred on the conductor ends. N_3 is shifted to the centre of the gap. With a height offset, N_2 is in focus position, while N_1 is defocused in positive Z-translation (focal position is shifted into the workpiece).

As the BLW parameter does melt a similar volume of copper, but not the exact same volume of copper. This has an impact on the cross-sectional area $A_{\varphi=90^\circ}$, because the results of the cross-sectional area $A_{\varphi=90^\circ}$ are additionally normalized relative to the ideal position (zero position) of the BLW and SSP parameter each. This ensures the best possible comparability. The results are shown in Fig. 13. For the ideal position, the standard deviations $\sigma_{SSP}(0) = 0,0318 \text{ mm}^2$ and $\sigma_{BLW}(0) = 0,0259 \text{ mm}^2$ are determined for ten welds each. For every positional deviation, step one sample is welded with SSP and BLW parameter each. Diagrams (a) and (c) identify the positional deviations in X- and Z-direction as relevant deviations for the cross-sectional area $A_{\varphi=90^\circ}$. Other positional deviations cause changes $\Delta A_{\varphi=90^\circ} < 10\%$. The results also indicate that BLW has a higher tolerance in all translational position deviations. This is a consequence of the larger and thus more stable keyhole (Fig. 12). While using SSP a gap up to $\Delta x = 0,6 \text{ mm}$ can be welded with $A_{\varphi=90^\circ} > 1$, with BLW it is possible for deviations up to $\Delta x = 0,8 \text{ mm}$. Height deviations up to $\Delta z = 1,5 \text{ mm}$ for SSP lead to $A_{\varphi=90^\circ} > 0,8 \text{ mm}^2$, whereas for BLW an $A_{\varphi=90^\circ} > 0,8 \text{ mm}^2$ is also achieved for $\Delta z = 2,5 \text{ mm}$.

In contrast to Gläbel's investigations [10], the results of test series B2 exhibit no negative effects on the cross-sectional area for an offset in the Y-direction of up to 2 mm and rotations around Y of up to 15° . In addition, the height offset has an impact in the presented test series. The results coincide regarding the influence of a gap and no influence of rotations around the X- and Z-axis. It should be noted that the boundary conditions (welding geometry, copper material, conductor geometry) of Gläbel [10] partly differ from the boundary conditions used in this test series B2 [10].

3.3 Impact of gap, height offset, welding path and conductor end geometry (Test series C)

In a further test series C, the identified, significant deviations — gap and height offset — are considered in

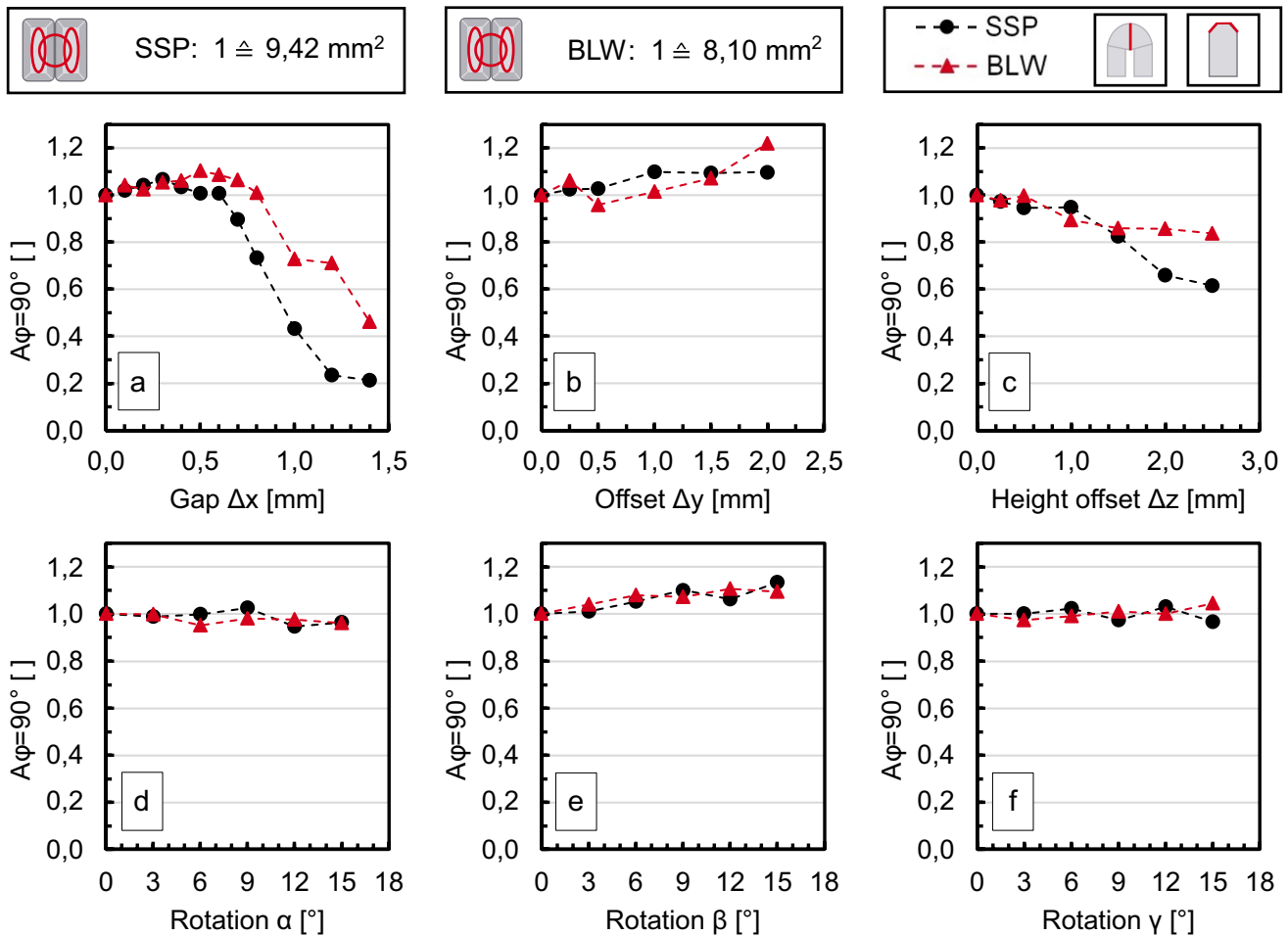


Fig. 13 Cross sectional area $A_{\varphi=90^\circ}$ for SSP and BLW as a function of translational and rotational degrees of freedom (Welding parameters: GEO 3—SSP and GEO 3—BLW) (Hairpins: Not cut, Cu-OF)

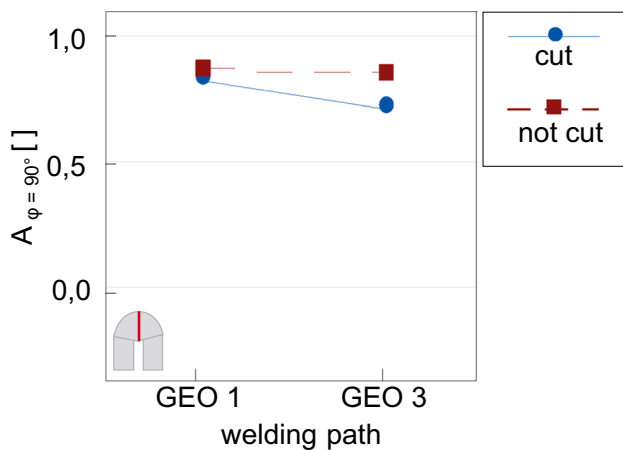


Fig. 14 Interaction plot (fitted mean values) of cross-sectional area $A_{\varphi=90^\circ}$; factors: conductor end geometry and welding path (Welding parameters: GEO 3—SSP and GEO 1—SSP) (Hairpins: Not cut and cut, Cu-OF)

combination with the conductor end geometry and welding path. Cu-OF and SSP are used. The reflectivity is measured 10 to 30% higher for hairpins that are cut again shortly before welding. The melt volume therefore decreases by 5% on average with the same energy input. The cross-sectional area $A_{\varphi=90^\circ}$ decreases on average by 1,4% for GEO 1 and by 2,8% for GEO 3. For this reason, the quality characteristics are normalized in this evaluation, equal to test series B. The averaged result from ten welded hairpin pairs with no positioning deviations (ideal position) is used as the reference for each combination of conductor end geometry and welding path.

First, the cross-sectional area of the pins is investigated. A significance level of $\alpha_3 = 0,05$ is set for the formation of the regression models (model equations and ANOVA: Appendix 3). Non-significant interactions (p -value $> 0,05$) are removed from the model equations. The results are normally distributed. The data values are checked for outliers using Grubbs' test ($\alpha_4 = 0,05$) [33]. No outliers are found.

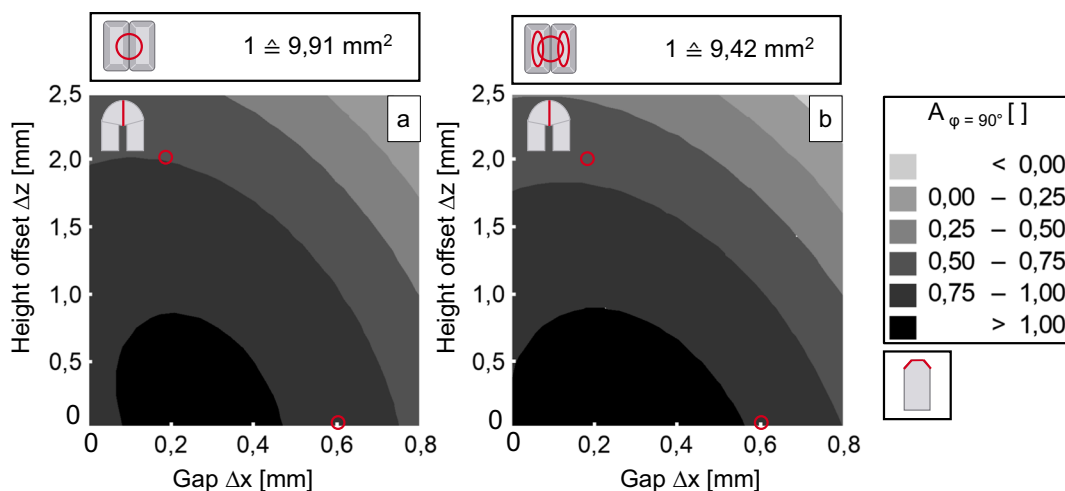


Fig. 15 Contour plot of Cross-sectional area $A_{\varphi=90^\circ}$; Factors: Height offset Δz , Gap Δx ; **a:** GEO 1; **b:** GEO 3 (Welding parameters: GEO 3—SSP and GEO 1—SSP) (Hairpins: Not cut, Cu-OF)

The model thus achieves a coefficient of determination R_{D3}^2 of 85,6%.

Figure 14 shows the interaction between the conductor end geometry and the welding path. For GEO 1, there is no difference in the cross-sectional area. For GEO 3, not-cut wire ends create a larger cross-sectional area. This is due to the chamfer, which results in a typical Y-seam (Fig. 4). The molten copper flows in the direction of the gap during the welding process and the weld depth increases. The adjusted mean value of the cross-sectional area of cut conductor ends thus decreases by 25,5%. For cut pins, the parameter GEO 1 is to be preferred.

For the further analysis of the factors, the not-cut conductor ends are used. Figure 15 illustrates the result of the cross-sectional area $A_{\varphi=90^\circ}$ in a contour plot for GEO 1 (a) and GEO 3 (b). First, it can be deduced that with an increasing height offset Δz and gap Δx , the cross-sectional area is reduced. A height offset leads to a lower energy density at the pin that remains outside the focal position. With an increasing gap, more energy is put into the gap instead of onto the conductor ends. For this reason, less copper is fused in both offset positions, so that the cross-sectional area is reduced. GEO 3 achieves a higher cross-sectional area for a gap than GEO 1. For

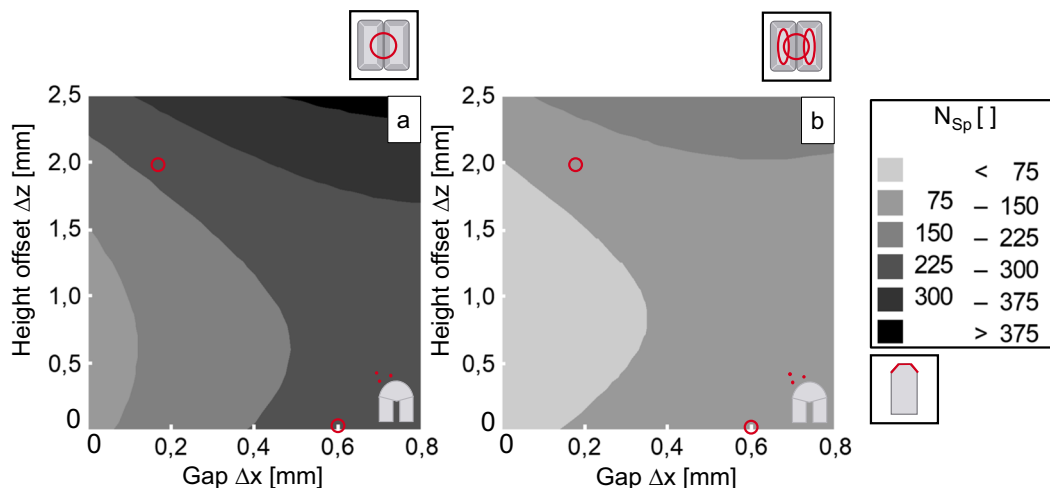


Fig. 16 Contour plot – number of welding spatters N_{Sp} ; Factors: Height offset Δz , Gap Δx ; **a:** GEO 1; **b:** GEO 3 (Welding parameters: GEO 3—SSP and GEO 1—SSP) (Hairpins: Not cut, Cu-OF)

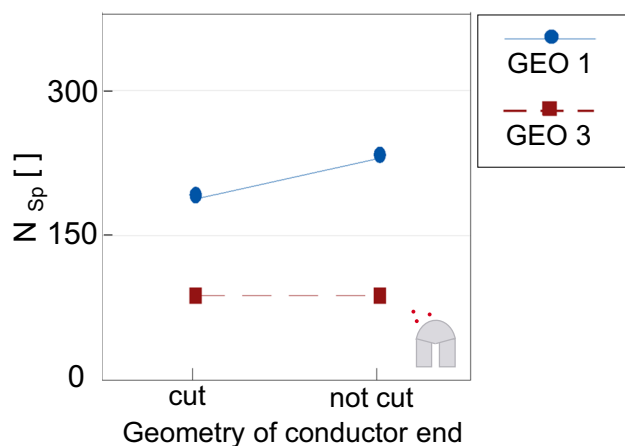


Fig. 17 Interaction plot (fitted mean values) of number of welding spatters N_{sp} ; Factors: conductor end geometry and welding path (Welding parameters: GEO 3—SSP and GEO 1—SSP) (Hairpins: Not cut and cut, Cu-OF)

$\Delta x = 0,6 \text{ mm}$ and $\Delta z = 0,0 \text{ mm}$, GEO 3 has a 6,7% higher cross-sectional area compared to GEO 1. For a height offset, GEO 1 achieves higher cross-sectional areas. For $\Delta x = 0,2 \text{ mm}$ and $\Delta z = 2,0 \text{ mm}$, there is a 9,5% higher cross-sectional area with GEO 1 compared to GEO 3.

The regression model from the analysis of spatter formation is presented below. (The results are normally distributed, no outliers according to Grubbs [33], significance level $\alpha_5 = 0,05$; model equations and ANOVA: Appendix 4). The coefficient of determination R_{D5}^2 is 89,9%. The values are not normalized because spatter formation does not directly depend on the generated melt volume and the process time of the parameters is almost equal ($t_p(\text{GEO } 1) = 109 \text{ ms}$, $t_p(\text{GEO } 3) = 112 \text{ ms}$). Figure 16 illustrates the result (a: GEO 1, b: GEO 3). Also, an increasing height offset and gap generate an increasing number of spatters N_{sp} . This is explained by the fact that high positional deviations can cause a collapse of the keyhole, which results in spatters. In particular, a gap between the conductor ends with a non-existent melt pool leads to an energy input on the insulation of the pins. This may damage the insulation. As GEO 3 initially creates a melt pool by melting the single pins first, the gap is bridged before N_3 . The laser only moves on existing melt. The keyhole thus remains more stable than with GEO 1. The offsets $\Delta x = 0,6 \text{ mm}$ and $\Delta z = 0,0 \text{ mm}$ result in a 112% higher number of spatters with GEO 1 compared to GEO 3, and for $\Delta x = 0,2 \text{ mm}$ and $\Delta z = 2,0 \text{ mm}$, in a 124% higher number of spatters.

The same effect is also shown in the interaction diagram (Fig. 17). For GEO 3 the conductor end geometry is not relevant due to the prior melting of the individual pins. For GEO 1 a gap $\Delta x > 0,2 \text{ mm}$ should be avoided and a cut conductor end geometry should be preferred. Also, the chamfer of the conductor ends can lead to a collapse of the keyhole in GEO 1.

4 Conclusion

Laser beam welding is already a favoured technology for hairpin welded joints. Many parameters must be considered in the process control that influence the welding result in various quality characteristics. The aim of the current study was to show the necessary requirements due to the electrical-thermal stress in a first step. In addition, the impact and behaviour of relevant influencing variables on the welding process should be clarified. Based on the series of tests carried out, the following conclusions are drawn:

- The connection area is a central quality characteristic for hairpin-welded joints in order to avoid thermal losses. It should be considered that pores can reduce the connection area. It is recommended to achieve a connection area larger than the cross-section of the copper wire. In further investigations, the mentioned requirements should be compared with the requirements resulting from dynamic vibrations of the electric drive.
- Dissolved oxygen in the copper generates increased porosity. The use of static beam shaping can reduce process pores in the hairpin welding process, as the gases can better dissipate from the keyhole. A more detailed description of the formation of process pores for hairpin welds is a future field of research. Therefore, an X-ray imaging during the welding process could be used.
- Of all the positional deviations, the gap and height offset are particularly relevant for the result of hairpin welding. By using static beam shaping, deviations in a larger range can be tolerated. Furthermore, it is confirmed that static beam shaping leads to a reduced number of spatters in the hairpin welding process.
- Under the use of the single spot welding, it is proven that a weld path with three geometries can bridge a gap better and causes less spatters. Additionally, for the number of spatters of three geometries there is no significant difference whether cut or not-cut pins are used. Only in the case of large height offsets of not-cut hairpins, one welding geometry reaches larger connection areas.

Appendix 1. Follow-up - ANOVA Test series A (Thermography)

Table 7

Table 7 ANOVA – test series A

| Test series A – temperature T | | |
|-------------------------------|--------|-----------------|
| Factors | SS | <i>p</i> -value |
| Quality level | 1000,0 | 0,000189 |
| Error | 698,4 | - |

Appendix 2. Follow-up – ANOVA Test series B1

Table 8

Table 8 ANOVA – test series B1

| Factors | SS | <i>p</i> -value |
|--|----------|-----------------|
| Test series B1 – pore volume V_p | | |
| Oxygen content | 0,069180 | 0,008173 |
| Static beam shaping (BLW) | 0,213162 | 0,000020 |
| Oxygen content · Stat. beam shaping | 0,009849 | 0,297848 |
| Error | 0,317748 | - |
| Test series B1 – volume of largest pore V_{pmax} | | |
| Oxygen content | 0,027205 | 0,063434 |
| Static beam shaping (BLW) | 0,150784 | 0,000067 |
| Oxygen content · Stat. beam shaping | 0,004319 | 0,450358 |
| Error | 0,266995 | - |
| Test series B1 – Number of spatters N_{Sp} | | |
| Oxygen content | 570,0 | 0,040072 |
| Static beam shaping (BLW) | 7425,6 | 0,000000 |
| Oxygen content · Stat. beam shaping | 34,2 | 0,604914 |
| Error | 4522,9 | - |

Appendix 3. Follow up – Regression Model for $A_{\varphi=90^\circ}$ in Test series C

Tables 9 and 10

Regression model for cross-sectional area $A_{\varphi=90^\circ}$:

$$A_{\varphi=90^\circ} = k_0 + k_1 \cdot \Delta z + k_2 \cdot \Delta x + k_3 \cdot \Delta z^2 + k_4 \cdot \Delta x^2 + k_5 \cdot \Delta x \cdot \Delta z \tag{5.}$$

Table 9 Coefficients of regression model for Cross-sectional area $A_{\varphi=90^\circ}$ – test series C

| | | Test series C—cross-sectional area $A_{\varphi=90^\circ}$ | | | | | |
|------------|-------|---|--------|--------|--------|--------|--------|
| Valid for: | | k_0 | k_1 | k_2 | k_3 | k_4 | k_5 |
| Cut | GEO 1 | 1,0254 | 0,0718 | 0,4320 | 0,0882 | 1,3280 | 0,2220 |
| Cut | GEO 3 | 0,9948 | 0,0091 | 0,4320 | 0,0882 | 1,3280 | 0,2220 |
| No cut | GEO 1 | 0,9478 | 0,0718 | 0,7349 | 0,0882 | 1,3280 | 0,2220 |
| No cut | GEO 3 | 1,0087 | 0,0091 | 0,7349 | 0,0882 | 1,3280 | 0,2220 |

Table 10 ANOVA – test series C – Cross-sectional area $A_{\varphi=90^\circ}$; *not considered in regression model; “no value”: no combination of height offset and cut pins possible

| Test series C—cross-sectional area $A_{\varphi=90^\circ}$ | | |
|---|----------|-----------------|
| Factors | SS | <i>p</i> -value |
| Regression model ($R_{D3}^2 = 85.6\%$) | 6,65597 | 0,000000 |
| Linear | 4,25509 | 0,000000 |
| Height offset Δz | 2,97193 | 0,000000 |
| Gap Δx | 1,35367 | 0,000000 |
| Welding path | 0,04869 | 0,018440 |
| Geometry of conductor end | 0,16064 | 0,000029 |
| Square | 1,04171 | 0,000000 |
| Δz^2 | 0,21727 | 0,000002 |
| Δx^2 | 0,95060 | 0,000000 |
| 2-factor interaction | 0,31767 | 0,000001 |
| $\Delta z \cdot \Delta x$ | 0,14543 | 0,000066 |
| $\Delta z \cdot$ welding path | 0,06553 | 0,006445 |
| $\Delta z \cdot$ Geometry of conductor end | No value | |
| $\Delta x \cdot$ welding path | * | 0,167402 |
| $\Delta x \cdot$ Geometry of conductor end | 0,18716 | 0,000007 |
| Welding path \cdot Geometry cond | 0,05226 | 0,014703 |
| Error | 0,64653 | 0,000000 |

Appendix 4. Follow up – Regression Modell for N_{Sp} in Test series C

Regression model for number of welding spatters N_{Sp}:
Tables 11 and 12

$$N_{Sp} = j_0 + j_1 \cdot \Delta z + j_2 \cdot \Delta x + j_3 \cdot \Delta z^2 + j_4 \cdot \Delta x^2 \quad (6.)$$

Table 11 Coefficients of regression model for number of welding spatters N_{Sp} – test series C

| | | Test series C—number of welding spatters N _{Sp} | | | | |
|------------|-------|--|----------------|----------------|----------------|----------------|
| Valid for: | | j ₀ | j ₁ | j ₂ | j ₃ | j ₄ |
| Cut | GEO 1 | 88,9 | 82,7 | 318,3 | 43,2 | 187,4 |
| Cut | GEO 3 | 46,9 | 72,5 | 235,1 | 43,2 | 187,4 |
| Not cut | GEO 1 | 130,7 | 52,7 | 318,3 | 43,2 | 187,4 |
| Not cut | GEO 3 | 46,0 | 72,5 | 235,1 | 43,2 | 187,4 |

Table 12 ANOVA – test series C – number of welding spatters N_{Sp}; * not considered in regression model; “no value”: no combination of height offset and cut pins possible

| Test series C—number of welding spatters N _{Sp} | | |
|--|----------|----------|
| Factors | SS | p-value |
| Regression model (R _{D5} ² of 89.9%) | 890946 | 0,000000 |
| Linear | 445324 | 0,000000 |
| Height offset Δz | 85042 | 0,000000 |
| Gap Δx | 160825 | 0,000000 |
| Welding path | 178436 | 0,000000 |
| Geometry of conductor end | 9810 | 0,000496 |
| Square | 84818 | 0,000000 |
| Δz ² | 52731 | 0,000000 |
| Δx ² | 19466 | 0,000002 |
| 2-factor interaction | 58325 | 0,000000 |
| Δz · Δx | * | 0,364615 |
| Δz · welding path | 6442 | 0,004448 |
| Δz · Geometry of conductor end | No value | |
| Δx · welding path | 18877 | 0,000002 |
| Δx · Geometry of conductor end | * | 0,668293 |
| Welding path · Geometry cond | 11322 | 0,000192 |
| Error | 33230 | 0,007936 |

Acknowledgements The authors would like to express their appreciation to Patrick Knecht (Porsche AG) for project support and Hermann Kaubitzsch (bgk infrarotservice GmbH), Daniel Passow (Universität Stuttgart—IEH), Jajnabalkya Guhathakurta (CT-Lab Stuttgart) for technical support.

Funding Open Access funding enabled and organized by Projekt DEAL.

Declarations

Conflict of interest The authors declare no competing interests.

Open Access This article is licensed under a Creative Commons Attribution 4.0 International License, which permits use, sharing, adaptation, distribution and reproduction in any medium or format, as long as you give appropriate credit to the original author(s) and the source, provide a link to the Creative Commons licence, and indicate if changes were made. The images or other third party material in this article are included in the article's Creative Commons licence, unless indicated otherwise in a credit line to the material. If material is not included in the article's Creative Commons licence and your intended use is not permitted by statutory regulation or exceeds the permitted use, you will need to obtain permission directly from the copyright holder. To view a copy of this licence, visit <http://creativecommons.org/licenses/by/4.0/>.

References

- Bibra E, Connelly E, Dhir S, Drtil M, Henriot P, Hwang I, Le Marois J, McBain S, Paoli L, Teter J (2022) Electric vehicle outlook 2022. IEA
- Verband der Automobilindustrie (2021) Erstes globales E-Mobility-Ranking. VDA, Berlin
- Nuzzo S, Barater D., Gerada C, Vai P (2021) Hairpin windings: an opportunity for next-generation E-motors in transportation. *IEEE Industrial Electronics Magazine*. <https://doi.org/10.1109/MIE.2021.3106571>
- Berardi G, Nategh S, Bianchi N, Thioliere Y (2020) A comparison between random and hairpin winding in e-mobility applications. *IECON 2020 The 46th Annual Conference of the IEEE Industrial Electronics Society*:815–820.<https://doi.org/10.1109/IECON43393.2020.9255269>
- Dr.-Ing. h.c. F. Porsche AG (2019) Stator mit Hairpin-Technologie im Taycan. *Porsche Christopherus Magazine* 392
- Glaessel T, Seefried J, Franke J (2017) Challenges in the manufacturing of hairpin windings and application opportunities of infrared lasers for the contacting process. *7th International Electric Drives Production Conference (EDPC)*:1–7. <https://doi.org/10.1109/EDPC.2017.8328150>
- Arzillo A, Braglia P, Nuzzo S, Barater D, Franceschini G, Gerada D, Gerada C (2020) Challenges and future opportunities of hairpin technologies. *IEEE 29th International Symposium on Industrial Electronics (ISIE)*:277–282. <https://doi.org/10.1109/ISIE45063.2020.9152417>
- Riedel A, Masuch M, Weigelt M, Gläfel T, Kühl A, Reinstein S, Franke J (2018) Challenges of the hairpin technology for production techniques. *21st International Conference on Electrical Machines and Systems (ICEMS)*:2471–2476.<https://doi.org/10.23919/ICEMS.2018.8549105>
- Dimatteo V, Ascari A, Faverzani P, Poggio L, Fortunato A (2021) The effect of process parameters on the morphology, mechanical strength and electrical resistance of CW laser-welded pure copper hairpins. *J Manuf Process* 62:450–457. <https://doi.org/10.1016/j.jmapro.2020.12.018>
- Gläfel T. (2020) Prozessketten zum Laserstrahlschweißen von flachleiterbasierten Formspulenwicklungen für automobiler Traktionsantriebe. Dissertation, FAU University Press
- Kampker A, Heimes H, Kawollek S, Treichel P, Kraus A (2019) Produktionsprozess eines Hairpinstators. *PEM of RWTH Aachen University*. <https://doi.org/10.13140/RG.2.2.26518.09285>
- Fleischer J, Hausmann L, Wirth F (2021) Production-oriented design of electric traction drives with hairpin winding. *Procedia CIRP* 100:169–174. <https://doi.org/10.1016/j.procir.2021.05.080>
- Heider A (2018) Erweitern der Prozessgrenzen beim Laserstrahlschweißen von Kupfer mit Einschweißstiefen zwischen 1 mm und 10 mm. Dissertation, Herbert Utz Verlag.
- Engler S, Ramsayer R, Poprawe R (2011) Process studies on laser welding of copper with brilliant green and infrared lasers. *Phys Procedia* 12:339–346. <https://doi.org/10.1016/j.phpro.2011.03.142>
- Speker N, Haug P, Feuchtenbeiner S, Hesse T, Havrilla D (2018) BrightLine weld-spatter reduced high speed welding with disk lasers. *High-Power Laser Mater Process: Appl, Diagn, Syst VII 105250:99–104*. <https://doi.org/10.1117/12.2287205>
- Bocksrocker O, Speker N, Beranek M, Hesse T (2019) Reduction of spatters and pores in laser welding of copper hairpins using two superimposed laser beams. *Laser in Manufacturing Conference Munich*.
- Omlor M, Racu AM, Hensel J, Dilger K (2022) Quality analysis of stripped wire contacts in the production of hairpin windings for electric drives. *31st International Conference on Electrical Contacts*.
- Glaessel T, Pinhal DB, Masuch M, Gerling D, Franke J (2019) Manufacturing influences on the motor performance of traction drives with hairpin winding. *Int Electr Drives Prod Conf (EDPC)* 9:1–8. <https://doi.org/10.1109/edpc48408.2019.9011872>
- Haug P, Weidgang S, Seebach J, Speker N, Hesse T, Bisch S (2019) Beam shaping BrightLine Weld—latest application results. *High-Power Laser Mater Process: Appl, Diagn, Syst VII 10911:207–214*. <https://doi.org/10.1117/12.2509560>
- Toth T, Hensel J, Thieme S, Sieber P, Dilger K (2021) Electron beam welding of rectangular copper wires applied in electrical drives. *Weld World* 65:277–2091. <https://doi.org/10.1007/s40194-021-01158-4>
- Deutsches Kupferinstitut (2019) Schweißen von Kupfer und Kupferlegierungen.
- Horrigan VM (1977) The solubility of oxygen in solid copper. *Metal Trans A* 8(5):785–787. <https://doi.org/10.1007/BF02664788>
- DIN EN (2013) Kupfer und Kupferlegierungen – Vordraht aus Kupfer 1977:2013
- Omlor M. Vorrichtung zur Herstellung eines Stators und vorgangintegrierten Prüfung einer Laserschweißnaht. Patent, Dr.-Ing. h.c. F. Porsche AG. DE10 2022 106 788, in press.
- Omlor M, Breitbarth A. Verfahren und Vorrichtung zur Prüfung eines Schweißbereichs. Patent, Dr.-Ing. h.c. F. Porsche AG. DE10 2022 101 024, in press
- Omlor M, Petrich T, Blumenstein C, Berndt C, Dilger K (2022) Method for analyzing welding speed and beam deflection and its effect on laser welded hairpin windings for electric drives. *Procedia Cirp* 111:551–556. <https://doi.org/10.1016/j.procir.2022.08.148>
- Omlor M, Guhathakurta J, Schmack T (2022) Verfahren zur Prüfung des Stators sowie Prüfungsanordnung zur Durchführung des Verfahrens. Patent, Dr.-Ing. h.c. F. Porsche AG. DE102021115391B3.
- Bernhard F. (eds) (2014) *Handbuch der Technischen Temperaturmessung*. Springer Vieweg, Berlin Heidelberg, 1163-1397. <https://doi.org/10.1007/978-3-642-24506-0>

29. Bliedtner J, Müller H, Barz A (2013) *Lasermaterialbearbeitung: Grundlagen – Verfahren – Anwendungen – Beispiele*. Carl Hanser Verlag GmbH & Co, KG, München, p 126
30. Schiebold K (2021) *Schweiß- und Lötverbindungen und ihre Prüfung*. Springer Fachmedien, Wiesbaden
31. Rapp HJ (1996) *Laserschweißbeignung von Aluminiumwerkstoffen für Anwendungen im Leichtbau*. Springer Fachmedien, Wiesbaden
32. TRUMPF (2019) BrightLine Wed: Perfekte Schweißergebnisse in Bestzeit. Flyer. https://www.trumpf.com/filestorage/TRUMPF_Master/Products/Lasers/02_Brochures/TRUMPF-disk-laser-BrightLineWeld-Flyer-DE.pdf. Accessed 01.10.2022
33. Grubbs FE (1969) Procedures for detecting outlying observations in samples. *Technometrics* 11:1–21. <https://doi.org/10.1080/00401706.1969.10490657>

Publisher's note Springer Nature remains neutral with regard to jurisdictional claims in published maps and institutional affiliations.